Azimuthal Variation in the Spectra of the 2019 Ridgecrest Earthquake Clusters and its Application to Understanding Fault Zone Structure

J. C. Neo[1], Y. Huang[1], D. Yao[2]

[1]University of Michigan, Ann Arbor
[2]China University of Geosciences, Wuhan

Corresponding author: Jing Ci Neo (neoj@umich.edu)

Key Points:

- Dynamic rupture simulations show that fault damage zones can amplify high-frequency waves close to fault strike direction.
- 93% of the M_L1.5-3 Ridgecrest clusters record more energy at 15-25 Hz for stations close to fault strike.
- We find that site effects cannot explain the azimuthal variation in the spectra of the Ridgecrest earthquakes.

This is a non-peer reviewed preprint submitted to EarthArXiv
This manuscript has been submitted to Geophysical Research Letters

Abstract

We first show through dynamic rupture models that FDZs can amplify high-frequency waves along directions close to fault strike and the amplified frequency band may be used to estimate the width and velocity contrast of the FDZ. Then, we identify this high-frequency amplification in the spectra of M1.5–3 earthquakes from the 2019 Ridgecrest earthquake sequence. We cluster the earthquakes by location and waveform similarity, and stack their velocity spectra to average source effects. We find that for 93% of the clusters, stations close to fault strike record more high-frequency energy at 15-25 Hz, close to the characteristic frequency of fault zone reflections. The results are consistent across clusters with average depths of 2.0–9.7km and average magnitudes of M1.6–2.7. Additionally, we analyze the relative site effects of the stations and find that they cannot explain the azimuthal variation in the spectra.

Plain Language Summary

Fault damage zones (FDZs) can influence how often large earthquakes occur and how devastating they can be. To estimate the properties of FDZs, researchers typically model waves that are trapped inside the FDZ. However, this method requires dense arrays located directly over the fault. Additionally, the depth of FDZs is still not well understood. Hence, we explore the possibility of inferring the characteristics of fault zones using seismic stations located at a distance. We analyze the frequency content of waves from M1.5-3 earthquakes in Ridgecrest, California. We find that stations located in the direction along the fault record more high-frequency energy than the other stations. Our simulations of the earthquakes show that the FDZ may have amplified the high-frequency energy through multiple reflections of the waves. The amplified frequency band could help us estimate the FDZ structure and wave velocities. Additionally, we find that the site effects (differences in shaking due to the site properties) cannot explain the azimuthal variation in the high frequency energy of earthquakes.

1. Introduction

Characterizing the structure of fault damage zones (FDZs) is important for the understanding of earthquake source physics and the evaluation of seismic hazard (Ben-Zion & Sammis, 2003; Rowe et al., 2013). The maturity of FDZs can influence the stress drop, ground motions, rupture extent, amount of slip, hypocenter locations, and recurrence intervals of earthquakes (e.g., Manighetti et al., 2007; Radiguet et al., 2009; Cappa et al., 2014; Perrin et al 2016; Abdelmeguid et al., 2019; Thakur et al 2020; Thakur & Huang 2021; Guo et al., 2022). Reflected and refracted waves within the FDZs also play an important role in modulating the rupture speed, slip rate, and rise time of large earthquakes (e.g., Harris & Day, 1997; Huang & Ampuero, 2011; Huang et al., 2014; Pelties et al., 2015; Weng et al., 2016). Thus, improving knowledge of the spatial extent of FDZs and their temporal evolution is a critical step to account for the effects of FDZs more accurately in models of earthquake rupture and cycles.

To characterize FDZ structure, current techniques usually utilize near-fault arrays to obtain a cross-sectional view at an array location. For example, the waveform modeling of fault zone trapped waves has been widely utilized to image the width and the shear wave velocity reduction of the FDZ (e.g., Lewis & Ben-Zion 2010; Li et al., 2014; Qiu et al., 2021), whereas fault zone head waves offer precise information on the velocity contrast across the fault interface at depth (e.g., McGuire & Ben-Zion, 2005; Zhao & Peng, 2008; Allam et al., 2014; Yang et al., 2015; Zheng et al., 2022). Waveform modeling of the reflection of body waves in FDZs has also been used to derive fault zone structure in high resolution (Li et al., 2007; Yang and Zhu 2010). More recently, high-quality data from dense, large-aperture across-fault arrays have made it possible to constrain fault zone structure using a variety of techniques, including passive and active sources (e.g., Hillers & Campillo, 2018; Modret et al., 2019; Wang et al., 2019; Yang et al 2020; Jiang et al 2021; Atterholt et al 2022; Share et al., 2022; She et al 2022; Song and Yang 2022; Zhou et al., 2022; Zhang et al 2023). However, it is still challenging to determine the depth of FDZs and the results may vary depending on the technique used (Yang, 2015; Zhang et al 2023). In addition, the dense seismic arrays required by current methods are only available in certain fault zones.

Huang et al (2016) showed that FDZs can act as waveguides, reflecting and amplifying high-frequency waves along directions close to fault strike. Unlike trapped waves which appear only when the seismic stations are close to the FDZ, these P-waves are reflected in the fault damage zones before propagating outside the damage zone. Thus, these P-wave reflections can be recorded by stations at different distances. Huang et al (2016) conducted kinematic simulations and investigated M2.1–3.1 earthquakes from the 2003 Big Bear earthquake sequence. They observed secondary peaks in the velocity spectra of an earthquake cluster which matched kinematic simulations of the reflected high-frequency waves. The secondary peaks were observed by stacking P-wave velocity spectra of earthquakes with highly similar waveforms, and the associated frequency band of the peaks may be used to estimate the width and velocity contrast of the FDZ. This method uses seismic stations located at a distance from the FDZ and may be able to image FDZs along its width and depth. However, the impact of fault zone amplification is difficult to separate from the rupture directivity effect. Studies typically attribute azimuthal variations in earthquake waveforms and spectra to the rupture directivity effect, even for relatively small earthquakes (e.g., Rubin & Gillard, 2000; Kane et al., 2013; Fan & McGuire, 2018; Lui & Huang, 2019; Pennington et al., 2023).

In this study, we hypothesize that the effect of fault zone amplification can be isolated by studying smaller earthquakes, i.e., M1.5–3 events. First, we compare the effects of fault zone amplification versus rupture directivity using dynamic rupture simulations. We find that for 120–200 m long ruptures and FDZ widths of ~300–400 m, fault zone amplification causes a secondary peak at 15–25 Hz in the normalized velocity spectra for stations close to fault strike, while rupture directivity does not. Earthquakes with shorter rupture lengths would lead to more focused high-frequency spectral peaks. Then, we conduct a large-scale study of M1.5–3 earthquakes to identify the high-frequency peak associated with fault zone waves in their stacked velocity spectra. We use stations at hypocentral distances of 0.1–1 deg in the 2019 Ridgecrest earthquake region. We cluster the Ridgecrest earthquakes by their locations and waveform similarity, calculate the velocity spectra from a 1 s window around the P arrival, and stack the spectra to average the source effects of individual earthquakes. We observe that the stations located in the direction along the fault record more high-frequency energy than the other stations. We also investigate the depth and magnitude dependency of the increase in high-frequency energy for different clusters. In addition, we compute the relative site effects of the stations. We find that the stations that primarily occur in Z1 do not have larger site amplification values than those in Z2, and that site effect cannot explain the azimuthal variation in the high frequency energy of the Ridgecrest earthquakes.

2. Dynamic rupture simulations

To understand how fault zone structure and rupture directivity affect P wave propagation for small earthquakes, we simulate mode II dynamic rupture on a 1-D fault embedded in a FDZ with 40% velocity reduction that is 2km long and 400m wide. We describe the other simulation parameters in the supplementary material. The resulting rupture length is 120–200m in our simulations, which equals the rupture lengths of M ~2.1–2.5 earthquakes assuming a circular crack model with a stress drop of 3MPa. We set stations for every 3.75 degrees at 15km away from the hypocenter, far enough to separate P and S waves. We calculate the P wave velocity spectra using a 1s window starting immediately before the first P arrival (Figure 1). The spectra show amplified high-frequency energy for stations that span ~20° from fault strike (hereafter denoted as zone 1, Z1), but not for stations outside zone 1 (e.g., stations that span ~30° from fault strike, hereafter denoted as zone 2, Z2). The model configuration is shown in Figure S1. We attribute this difference in velocity spectra to the P wave reflections in FDZs recorded by Z1 stations. The frequency bands associated with fault zone waves are affected by the widths and velocity contrasts of FDZs, with larger widths and smaller velocity contrasts leading to lower frequency bands (Figure S2).

Though Huang et al., (2016) observed a similar result using kinematic models with point sources, the dynamic rupture simulations further illustrate the effects of finite rupture lengths. Shorter earthquake rupture leads to a more focused high-frequency spectral peak between 15–22Hz (Figure 1A), whereas high-frequency energy radiated by longer rupture is more spread out between 15–30Hz (Figure 1B), which manifests the interplay between rupture propagation and fault zone waves. Such high-frequency spectral peaks, however, are not observed for rupture with similar lengths in a homogeneous medium (Figure 1C). Though for homogenous rupture with lengths less than 200m, velocity spectra for Z1 stations may have larger amplitudes than Z2 stations due to rupture directivity (Figure S3), their normalized spectra are lower than those for Z2 stations within 15–22Hz. Further inspection of homogenous rupture simulations shows that extra high-frequency energy associated with rupture directivity is observed at frequencies higher than 35 Hz for 150m long rupture and 22Hz for 200m long rupture in the normalized velocity spectra (Figure 1D).

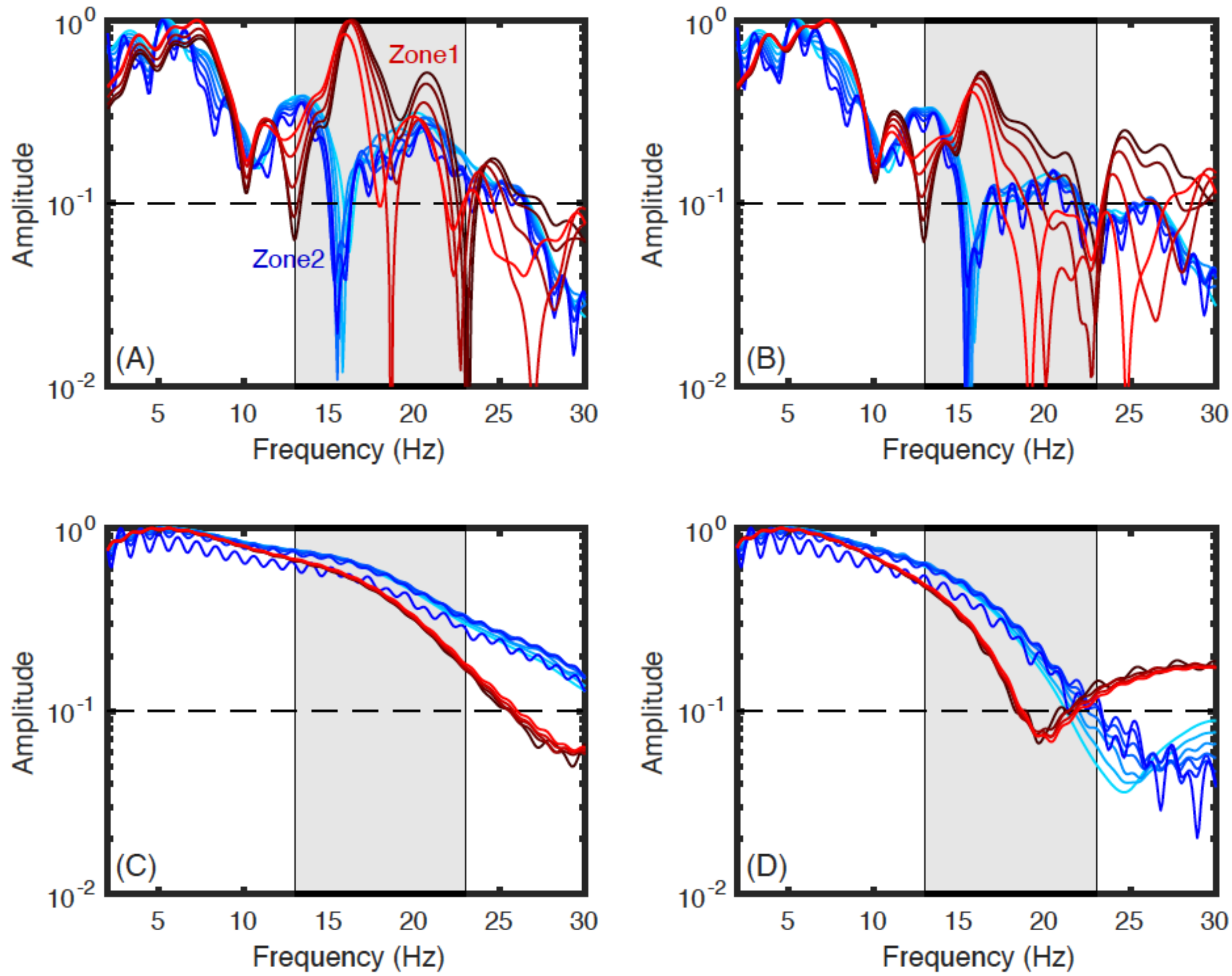

Figure 1. Normalized P wave velocity spectra for Z1 (red) and Z2 (blue) stations for (A and B) 120 m and 150 m long rupture inside a fault damaged zone, (C and D) 150 m and 200 m long rupture in a homogeneous medium. The gray region denotes the approximate frequency range of extra high-frequency P-wave energy recorded by Z1 stations.

3. Seismic Data Analysis

To obtain the earthquake clusters, we use earthquake locations recorded in the updated 1981-2022 SCEDC waveform relocated catalog (Hauksson et al., 2012). There are a total of 14,219 M1.5–3 earthquakes in the region spanning 35.5 to 36.0N and -117.8 to -117.3E for the period of 1 Jan 2019 – 4 Aug 2022. We use small earthquakes as the FDZ widths should be larger than rupture lengths to observe the extra high frequency energy caused by fault zone waves, and small earthquakes are less likely to exhibit rupture directivity (Kane et al 2013). We cluster the earthquakes by epicentral distances, where all earthquakes in each cluster are within 500 m of all other events in the cluster (example in Figure S4A). We select clusters with at least 15 events and download waveform data for the 4,431 events with IRIS Fetchdata (see Data Availability). We use velocity seismograms from broadband stations and geophones (DPZ, EHZ, HHZ) located at 0.1–1deg, excluding the A and B array stations of the 3J network as their spectra differ significantly across each array. We remove the instrument response for DPZ stations, because unlike other stations, their response is not flat for our frequency band of interest (1–30Hz).

We pick the P-wave arrivals using the STA/LTA method and cut a 1s time window before and after the first P-wave arrival to calculate signal-to-noise ratios (SNRs), keeping the events with SNR > 2. We also apply automatic gain control to the waveforms and align the waveforms using multi-channel cross-correlation. We then calculate the cross-correlation coefficients (cc) of all event pairs in each cluster for a frequency band of 2-8 Hz and keep the events with cc > 0.7 with at least 7 other events in the cluster. We select clusters with a minimum of 7 events recorded by at least 3 stations. Finally, we calculate the P-wave velocity spectra for each station using a 1 s time window, and stack and smooth the spectra. Details of these steps including the filters and time windows are outlined in Table S1.

Based on our simulation results, we define the zone that spans 20° from fault strike as Z1, and the rest as Z2, using the strike of the 2019 M_w7.1 Ridgecrest mainshock, 318°. Using variable strikes derived from focal mechanisms of individual events has a minimal effect on our results (details in Section 4.1). As shown by the results of a cluster in Figure 2, there can be some variation in the spectra of each event. For example, one of the events in the example cluster has much lower amounts of high-frequency energy than the others (Figure 2B-G, waveforms in Figure S4B-G), which may be due to wave attenuation and site effects. We will discuss this in Section 5.1.

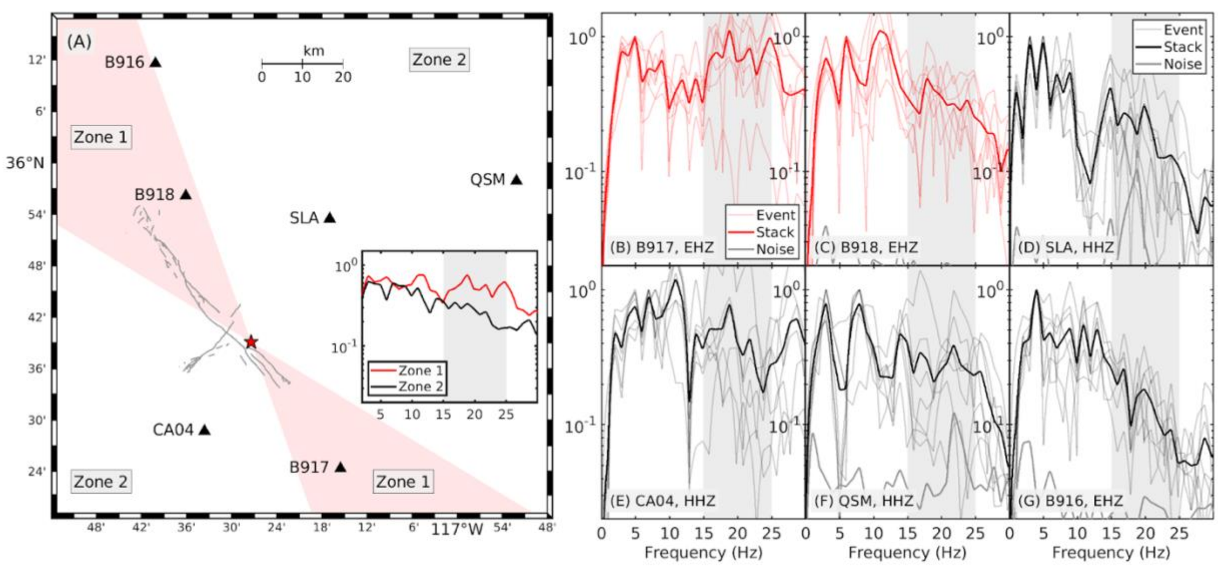

Figure 2: (A) Map of the stations for one example cluster. The red star indicates the location of the cluster while black triangles represent the stations. The inset map shows the stack of the spectra from each zone. The normalized P-wave velocity spectra of the events in the example cluster are plotted for Z1 (B-C) and Z2 (D-G) stations.

To quantify the increase in high-frequency energy for Z1 stations, we select a low-frequency (LF) band of 5–15Hz and a high-frequency (HF) band of 15–25Hz, which is close to the frequency band of extra high-frequency in dynamic rupture simulations. We also test different frequency bands, and the results are detailed in Section 4.1. To interpret our results, we define two "amplification ratios", r_stn and r_clus. r_stn is the amplification ratio for each station in a cluster and is defined as the ratio of the average HF to LF stacked spectral amplitudes. r_clus represents the amplification ratio for the cluster and is calculated using the ratio of the average r_stn values of Z1 to Z2. r_clus > 1 means that the clusters have larger average HF/LF ratios in Z1 compared to Z2. Our simulations suggest that there should be minimal amplification from the fault zone if the cluster is located outside of or beneath the FDZ. Hence, we would expect clusters within the FDZ to have r_clus values > 1 and other clusters to be ~1.

4. Results

We obtain 140 clusters, and Figure 3A shows the number of events and stations for each cluster. Approximately 54% of the clusters are recorded by 3–4 stations, 30% by 5–6 stations, and 16% by more than 6 stations. The average depths of the clusters range from 2.0–9.7km, and the average magnitudes of the clusters range from 1.6–2.4, except one cluster with an average magnitude of 2.7. Most of the clusters are located close to the mainshock fault trace, with two clusters further away on the foreshock fault trace.

4.1 Higher Ratios in Z1 for Most Clusters

As shown by the r_clus values of the 140 clusters (Figure 3B), 93% of the clusters have r_clus values higher than 1. This means that the clusters have larger average HF/LF ratios in Z1 compared to Z2. Unexpectedly, the two clusters near the orthogonal foreshock fault trace have r_clus values higher than 1. However, detailed analysis of the Ridgecrest aftershocks has revealed multiscale orthogonal faults throughout the region (Ross et al., 2019). These clusters could be located on a fault plane with the same orientation as the mainshock fault plane, or at the intersection of multiple fault planes.

To verify our results, we conduct a range of parameter tests to further understand the dependency of our results on frequency band, fault strikes, and station zone widths. We test LF bands of 3–10 Hz and 3–15 Hz as well as HF bands of 10–25 Hz and 10–20 Hz. The results are similar for each combination, where at least 84% of the r_clus values are higher than 1. Next, we determine the average strike of each cluster based on the focal mechanisms from Cheng et al. (2021) if more than half of the strikes fall within a 20° range. Using this method, we evaluate the average strike of 86 of the clusters and assume a fixed strike of 318° for the rest. We find that 103 clusters out of 115 (89.6%) have r_clus values higher than 1. The tests suggest that our results are robust to the frequency bands and fault strike. To evaluate the suitability of our station zone widths, we plot the r_stn values for all clusters superimposed on each other with each cluster centered at the origin (Figure S5). The azimuthal trend shown in Figure S5 suggests that defining Z1 to be 20 degrees captures most of the higher r_stn values in Z1. It is also clear from Figure S5 that the complexities of a fault damage zone and high frequency energy cannot be fully captured by the simplistic way that we are defining the zones. Nevertheless, our method is able to provide a meaningful starting point for further exploration and analysis.

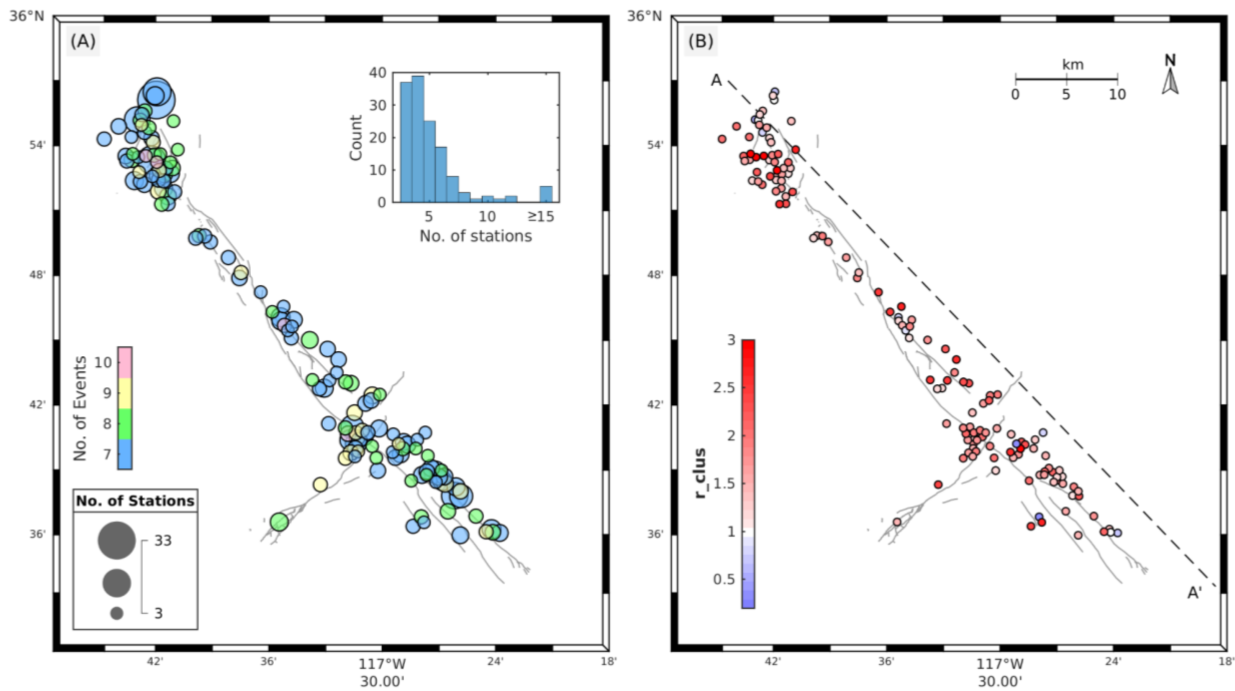

Figure 3: (A) The map displays all event clusters, with colors indicating the number of events and size reflecting the number of stations. A histogram in the inset illustrates the distribution of the number of stations recording each cluster. (B) Plot of r_clus values for each cluster, as indicated by the color of the circles. The Ridgecrest main fault trace is depicted by gray lines. The A-A' line has a strike of 318°.

4.2 Trends in Depth and Magnitude

To investigate any potential change in fault zone properties with depth, we plot the r_clus values with average depth of the cluster in Figure 4B. The r_clus values increase slightly with the average depth of the clusters. This trend may be caused by higher attenuation near the surface (Frankel & Wennerberg, 1989; Abercrombie, 1997), making the fault zone amplification effect less pronounced. However, the trend is relatively small and may not be significant. We also examine the variation of r_clus values with magnitude (Figure 4C), and find that the ratios do not vary with the average magnitude of the clusters.

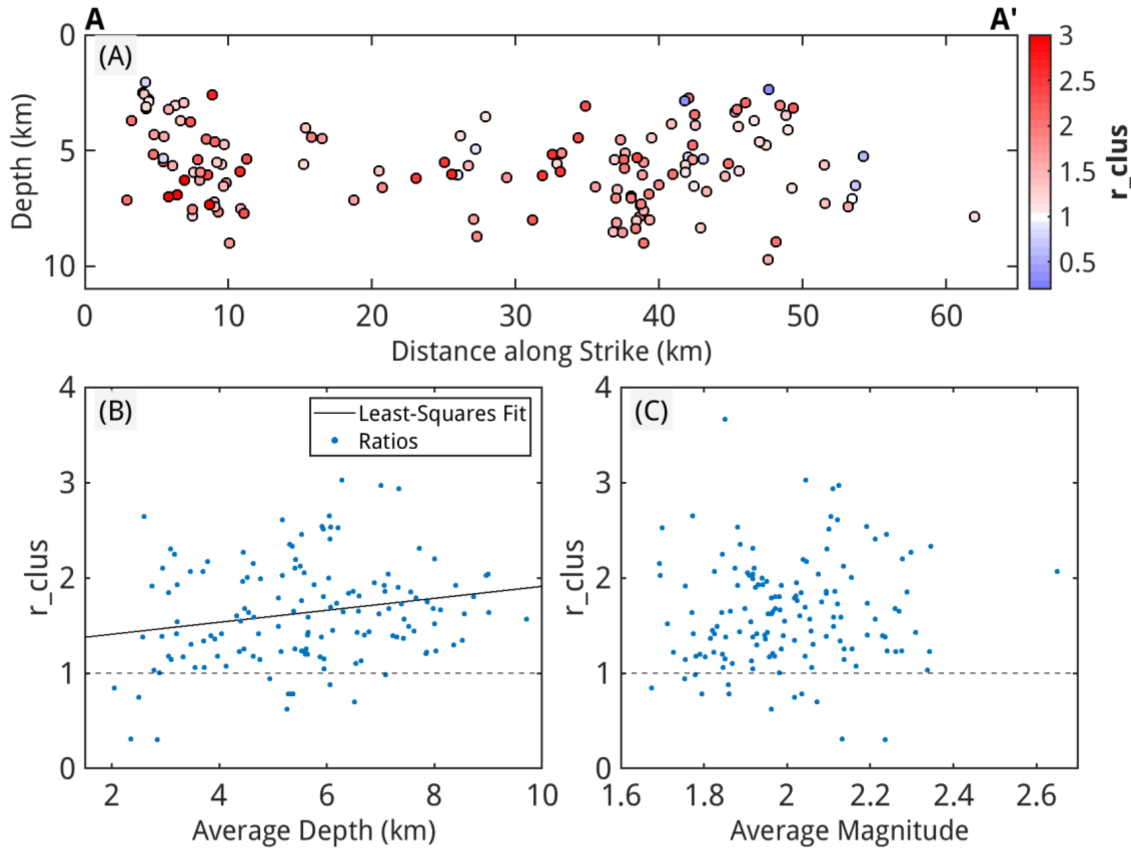

Figure 4: Amplification ratios as a function of depths and magnitudes of the clusters. (A) The clusters are projected along the A-A' line in Figure 1 and plotted along strike and depth. They are colored by their amplification ratios. (B) Plot of the amplification ratios of the clusters against average depths of the clusters. The black line shows the least-squares fit. (C) Plot of the amplification ratios of the clusters against average magnitudes of the clusters.

In summary, we observe an azimuthal variation in the stacked velocity spectra of earthquakes along the Ridgecrest fault traces. We interpret it as due to the amplification of seismic waves propagating in FDZs surrounding the fault strands that each cluster is located on. Our results suggest there are multiple FDZs present throughout the region that can extend up to depths of ~10km (Figure 4A) along most of the main fault trace.

5. Discussion

5.1 Investigation of site effects

The site effect at each station could affect our results as the stations are located over different rock types and some are over fault damage zones. For example, sedimentary layers have been shown to amplify ground motions at different frequencies (e.g., Li et al 2023). Furthermore, we use stations from different networks, including borehole stations and geophone arrays (summarized in Table S2). Borehole stations could record more high frequency signals than stations located near the surface, although the geophones used in this study have been shown to be comparable to borehole stations (Catchings et al., 2020).

Rock type is often categorized using Vs30 (Boore et al., 1993; Rusydi et al., 2018), where larger Vs30 values correspond to harder rock and less amplification of high-frequency ground motions. Therefore, we investigate the correlation of Vs30 (Thompson, 2018) and instrument type on our results (Figure S6A in the Supplementary). We interpolate to obtain the Vs30 values at the location of each station. We average the r_stn values for each station across all clusters and plot them against Vs30 (Figure S6B). There is no trend in the average r_stn values with Vs30, and a slight decreasing trend for station distance from fault trace (Figure S6C) which is likely due to the attenuation with distance. High-frequency attenuation would affect our results if the Z1 stations are located closer than the Z2 stations. However, our Z1 stations have a larger average station distance (43.4km) compared to the Z2 stations (36.0km). We also plot the average r_stn values for each network (Figure S6D), and they display a similar range of values.

To account for site effect and station response, we calculate the “relative site effects” of the stations using the spectral ratio method (Song and Yang 2022), with details in Text S2. We use 5 regional events (Table S3), each recorded by a subset of the stations, to compute the r_stn values from those events for 46 out of 55 of the stations used in our study (Figure S7). We invert for the relative site effects (r_site) using the following equations (M is number of stations):

$$r\_diff_{i,j} = r\_stn_i - r\_stn_j \tag{1}$$

$$\begin{bmatrix} 1 & -1 & 0 & 0 & \dots & 0 & 0 \\ 1 & 0 & -1 & 0 & \dots & 0 & 0 \\ \dots & \dots & \dots & \dots & \dots & \dots & \dots \\ 0 & 0 & 0 & 0 & \dots & 1 & -1 \end{bmatrix} \times \begin{bmatrix} r\_site_1 \\ r\_site_2 \\ \dots \\ r\_site_M \end{bmatrix} = \begin{bmatrix} r\_diff_{1,2} \\ r\_diff_{1,3} \\ \dots \\ r\_diff_{M-1,M} \end{bmatrix} \tag{2}$$

We find that the r_site values do not have any trend with geographical location or azimuth (Figure S8). The 3J, 7Q and GS networks have similar values, likely because their stations overlap geographically (Figure S9). The CI network has the largest spread in r_site values, likely because its stations are located the furthest apart. The borehole network (PB) has consistently average-to-lower r_site values. Crucially, the r_site values are similar for stations primarily in Z1 and those that are mostly in Z2 (Figure S9). However, it is still possible that the four Z1 stations with higher ratios are dominating the results. Hence, we reanalyze the clusters without these stations (Figure S10), and find that most clusters do not include them.

5.2 Is the azimuthal variation caused by fault zone amplification, or rupture directivity?

As shown by the dynamic rupture simulations, we can distinguish between fault zone amplification and rupture directivity using the normalized velocity spectra of small earthquakes. Moreover, corner frequencies of M < 2 earthquakes are likely larger than ~20 Hz for the 2019 Ridgecrest sequence (Trugman, 2020). Thus, the impact of rupture directivity is likely to be minimal for the

HF band we use (15–25Hz), especially for the clusters with smaller average magnitudes. In addition, if the rupture directivity effect is present in our results, we would expect to see increasing r_clus with magnitude, depending on the frequency band. The consistency of our results across different magnitudes suggests that the impact of rupture directivity is minimal.

On the other hand, the stacked spectra of Z1 stations appears to contain more high-frequency energy for Z1 stations to the Southeast (SE) than to the Northwest (NW). By averaging the r_stn values of the Z1 stations on each end of the fault, we find that 18 out of 20 clusters have higher average r_stn values to the SE than to NW. This seems to suggest that a large majority of our events exhibit SE rupture directivity. However, this observation is biased by the insufficient station coverage to the NW (only 3 stations). Further examination reveals that the lower r_stn values to the NW are largely due to one station (PB) B916 on the northern edge of the zone. The other two NW stations, (3J) R11 and (7Q) RCW07, have consistently higher r_stn values than average. Therefore, the apparent rupture directivity is likely due to limited station coverage to the NW.

5.3 Comparison with Ridgecrest FDZ imaging studies

The Ridgecrest FDZ has been imaged with a variety of techniques. Qiu et al. (2021) imaged the Ridgecrest FDZ using P-wave delay time, S-wave amplification, and fault zone trapped waves recorded by the dense B arrays from the RAMP deployment located directly over the fault trace. They found several 1–2 km wide low-velocity zones beneath each array, and 0.5-1.5 km wide more intensely damaged inner cores. Zhou et al. (2021) applied ambient noise tomography to the region and their results show a heterogenous, flower shaped FDZ up to 5 km wide and ~5 km in depth, with average velocity reduction of 40%. Rodriguez Padilla et al. (2022) analyzed data from aftershocks, strain maps, post-earthquake lidar data, and rupture maps. Based on the fracture density distribution of the FDZ, they predict a decrease in shear modulus by ~40% in sediment immediately adjacent to the fault, and a decrease by ~20% in bedrock, which declines to <1% at 100m away from the fault. In our study, we observed wave amplification at 15–25 Hz. Assuming a P-wave velocity of 6 km/s in the host rock and a velocity reduction of 40%, this implies that the FDZ has a width of ~144-240 m, which is similar to the more intensely damaged inner cores found by Qiu et al. (2021) and the FDZ width observed by Rodriguez Padilla et al. (2022).

6. Conclusion

Through analyzing the azimuthal variation in the stacked P-wave velocity spectra of the M1.5-3 Ridgecrest aftershocks, we investigate a possible source of high-frequency energy that has not been well understood. We observe that for 93% of our clusters, stations close to the fault strike record more high-frequency energy around 15–25 Hz compared to the other stations. This observation remains consistent across varying magnitudes, suggesting minimal influence from rupture directivity. As demonstrated by our dynamic rupture simulations, the associated frequency band is close to the characteristic frequency of fault zone reflections. We also calculate the relative site effects for most of our stations, and find that they cannot explain the azimuthal variation in the Ridgecrest earthquake spectra. We propose that the azimuthal variation is due to fault zone amplification, and the Ridgecrest FDZ could extend to a depth of 10km along most of the main fault trace. Our method presents a new way to study fault zone structure at depth, with broad applicability to other regions instrumented by broadband seismometers.

Acknowledgements

We thank editor Germán Prieto, and two reviewers (Hongfeng Yang and an anonymous reviewer) for their critical and constructive feedback. JCN and YH acknowledge funding from the NSF grant EAR-1943742.

Open Resource

We utilized waveforms and metadata from the CI (California Institute of Technology & United States Geological Survey Pasadena, 1926), NN (University of Nevada Reno, 1971), GS (Albuquerque Seismological Laboratory (ASL)/USGS, 1980), PB (Plate Boundary Observatory Borehole Seismic Network, 2004), 3J (Steidl et al., 2019), and 7Q (Ghosh, A., 2019) networks.

References

Abdelmeguid, M., Ma, X., & Elbanna, A. (2019), A novel hybrid finite element-spectral boundary integral scheme for modeling earthquake cycles: Application to rate and state faults with low-velocity zones. Journal of Geophysical Research: Solid Earth, 124(12), 12854-12881.

Abercrombie, R. E. (1997), Near-surface attenuation and site effects from comparison of surface and deep borehole recordings. Bulletin of the Seismological Society of America, 87(3), 731-744.

Albuquerque Seismological Laboratory (ASL)/USGS (1980), US Geological Survey Networks [Data set]. International Federation of Digital Seismograph Networks. https://doi.org/10.7914/SN/GS

Allam, A. A., Ben-Zion, Y., & Peng, Z. (2014), Seismic imaging of a bimaterial interface along the Hayward fault, CA, with fault zone head waves and direct P arrivals. Pure and Applied Geophysics, 171, 2993-3011.

Ampuero, J. P. (2009), SEM2DPACK: A spectral element method tool for 2D wave propagation and earthquake source dynamics, User's Guide, version 2.3.6. Retrieved from http://www.sourceforge.net/projects/sem2d/

Atterholt, J., Zhan, Z., & Yang, Y. (2022). Fault Zone Imaging With Distributed Acoustic Sensing: Body-To-Surface Wave Scattering. Journal of Geophysical Research: Solid Earth, 127(11), e2022JB025052.

Ben-Zion, Y., & Sammis, C. G. (2003), Characterization of fault zones. Pure and applied geophysics, 160, 677-715.

Boore, D. M., Joyner, W. B., & Fumal, T. E. (1993), Estimation of response spectra and peak accelerations from western North American earthquakes: an interim report.

California Institute of Technology and United States Geological Survey Pasadena. (1926), Southern California Seismic Network [Data set]. International Federation of Digital Seismograph Networks. https://doi.org/10.7914/SN/CI

Cappa, F., Perrin, C., Manighetti, I., & Delor, E. (2014), Off-fault long-term damage: A condition to account for generic, triangular earthquake slip profiles. Geochemistry, Geophysics, Geosystems, 15(4), 1476-1493.

Catchings, R. D., Goldman, M. R., Steidl, J. H., Chan, J. H., Allam, A. A., Criley, C. J., ... & Ben-Zion, Y. (2020), Nodal seismograph recordings of the 2019 Ridgecrest earthquake sequence. Seismological Society of America, 91(6), 3622-3633.

Cheng, Y., Ross, Z. E., Hauksson, E., & Ben-Zion, Y. (2021), A Refined Comprehensive Earthquake Focal Mechanism Catalog for Southern California Derived with Deep Learning Algorithms, S32A-05] presented at 2021 Fall Meeting, AGU, 15 Dec.

Fan, W., & McGuire, J. J. (2018), Investigating microearthquake finite source attributes with IRIS Community Wavefield Demonstration Experiment in Oklahoma. Geophysical Journal International, 214(2), 1072-1087.

Frankel, A., & Wennerberg, L. (1989), Microearthquake spectra from the Anza, California, seismic network: site response and source scaling. Bulletin of the Seismological Society of America, 79(3), 581-609.

Ghosh, A. (2019), RAPID: Capturing aftershock sequence of 2019 Mw 6.4 Ridgecrest and 7.1 Ridgecrest earthquakes [Data set]. International Federation of Digital Seismograph Networks. https://doi.org/10.7914/SN/7Q_2019

Guo, H., Lay, T., & Brodsky, E. E. (2022), Seismological Indicators of Geologically Inferred Fault Maturity. Authorea Preprints.

Harris, R. A., & Day, S. M. (1997), Effects of a low-velocity zone on a dynamic rupture. Bulletin of the Seismological Society of America, 87(5), 1267-1280.

Hauksson, E., Yang, W., & Shearer, P. M. (2012), Waveform relocated earthquake catalog for southern California (1981 to June 2011). Bulletin of the Seismological Society of America, 102(5), 2239-2244.

Huang, Y., & Ampuero, J. P. (2011), Pulse-like ruptures induced by low-velocity fault zones. Journal of Geophysical Research: Solid Earth, 116(B12).

Huang, Y., Ampuero, J. P., & Helmberger, D. V. (2014), Earthquake ruptures modulated by waves in damaged fault zones. Journal of Geophysical Research: Solid Earth, 119(4), 3133-3154.

Huang, Y., Ampuero, J. P., & Helmberger, D. V. (2016). The potential for supershear earthquakes in damaged fault zones–theory and observations. Earth and Planetary Science Letters, 433, 109-115.

Hillers, G., & Campillo, M. (2018), Fault zone imaging from correlations of aftershock waveforms. Pure and Applied Geophysics, 175, 2643-2667.

Jiang, X., Hu, S., & Yang, H. (2021). Depth extent and Vp/Vs ratio of the Chenghai fault zone, Yunnan, China constrained from dense-array-based teleseismic receiver functions. Journal of Geophysical Research: Solid Earth, 126(8), e2021JB022190.

Kane, D. L., Shearer, P. M., Goertz-Allmann, B. P., & Vernon, F. L. (2013), Rupture directivity of small earthquakes at Parkfield. Journal of Geophysical Research: Solid Earth, 118(1), 212-221.

Lewis, M. A., & Ben-Zion, Y. (2010), Diversity of fault zone damage and trapping structures in the Parkfield section of the San Andreas Fault from comprehensive analysis of near fault seismograms. Geophysical Journal International, 183(3), 1579-1595.

Li, X., Huang, Y., Chen, Z., & Huang, X. (2023). Effects of the accretionary wedge and sedimentary layers on subduction zone earthquake ruptures and ground motion: 2-D numerical simulations. Geophysical Journal International, 232(3), 2049-2069.

Li, Y. G., De Pascale, G. P., Quigley, M. C., & Gravley, D. M. (2014), Fault damage zones of the M7. 1 Darfield and M6. 3 Christchurch earthquakes characterized by fault-zone trapped waves. Tectonophysics, 618, 79-101.

Lui, S. K., & Huang, Y. (2019), Do Injection-Induced Earthquakes Rupture Away from Injection Wells due to Fluid Pressure Change? Do Injection-Induced Earthquakes Rupture Away from Injection Wells. Bulletin of the Seismological Society of America, 109(1), 358-371.

Manighetti, I., Campillo, M., Bouley, S., & Cotton, F. (2007), Earthquake scaling, fault segmentation, and structural maturity. Earth and Planetary Science Letters, 253(3-4), 429-438.

McGuire, J., & Ben-Zion, Y. (2005), High-resolution imaging of the Bear Valley section of the San Andreas Fault at seismogenic depths with fault-zone head waves and relocated seismicity. Geophysical Journal International, 163(1), 152-164.

Mordret, A., Roux, P., Boué, P., & Ben-Zion, Y. (2019), Shallow three-dimensional structure of the San Jacinto fault zone revealed from ambient noise imaging with a dense seismic array. Geophysical Journal International, 216(2), 896-905.

Neo, J. C., Fan, W., Huang, Y., & Dowling, D. (2022), Frequency-difference backprojection of earthquakes. Geophysical Journal International, 231(3), 2173-2185.

Pelties, C., Huang, Y., & Ampuero, J. P. (2015), Pulse-like rupture induced by three-dimensional fault zone flower structures. Pure and Applied Geophysics, 172, 1229-1241.

Pennington, C. N., Wu, Q., Chen, X., & Abercrombie, R. E. (2023), Quantifying rupture characteristics of microearthquakes in the Parkfield Area using a high-resolution borehole network. Geophysical Journal International, 233(3), 1772-1785.

Perrin, C., Manighetti, I., Ampuero, J. P., Cappa, F., & Gaudemer, Y. (2016), Location of largest earthquake slip and fast rupture controlled by along-strike change in fault structural maturity due to fault growth. Journal of Geophysical Research: Solid Earth, 121(5), 3666-3685.

Qiu, H., Ben-Zion, Y., Catchings, R., Goldman, M. R., Allam, A. A., & Steidl, J. (2021), Seismic imaging of the Mw 7.1 Ridgecrest earthquake rupture zone from data recorded by dense linear arrays. Journal of Geophysical Research: Solid Earth, 126(7), e2021JB022043.

Radiguet, M., Cotton, F., Manighetti, I., Campillo, M., & Douglas, J. (2009), Dependency of near-field ground motions on the structural maturity of the ruptured faults. Bulletin of the Seismological Society of America, 99(4), 2572-2581.

Rodriguez Padilla, A. M., Oskin, M. E., Milliner, C. W., & Plesch, A. (2022). Accrual of widespread rock damage from the 2019 Ridgecrest earthquakes. Nature Geoscience, 15(3), 222-226.

Ross, Z. E., Idini, B., Jia, Z., Stephenson, O. L., Zhong, M., Wang, X., ... & Jung, J. (2019), Hierarchical interlocked orthogonal faulting in the 2019 Ridgecrest earthquake sequence. Science, 366(6463), 346-351.

Rowe, C. D., Moore, J. C., Remitti, F., & IODP Expedition 343/343T Scientists. (2013), The thickness of subduction plate boundary faults from the seafloor into the seismogenic zone. Geology, 41(9), 991-994.

Rubin, A. M., & Gillard, D. (2000), Aftershock asymmetry/rupture directivity among central San Andreas fault microearthquakes. Journal of Geophysical Research: Solid Earth, 105(B8), 19095-19109.

Rusydi, M., & Efendi, R. (2018), Earthquake hazard analysis use Vs30 data in Palu. In Journal of Physics: Conference Series (Vol. 979, No. 1, p. 012054). IOP Publishing.

Share, P. E., Qiu, H., Vernon, F. L., Allam, A. A., Fialko, Y., & Ben-Zion, Y. (2022), General Seismic Architecture of the Southern San Andreas Fault Zone around the Thousand Palms Oasis from a Large-N Nodal Array. The Seismic Record, 2(1), 50-58.

She, Y., Yao, H., Yang, H., Wang, J., & Feng, J. (2022). Constraining the depth extent of low-velocity zone along the Chenghai Fault by dense array ambient noise interferometry and horizontal-to-vertical spectral ratio. Tectonophysics, 827, 229265.

Song, J., & Yang, H. (2022). Seismic site response inferred from records at a dense linear array across the Chenghai fault zone, Binchuan, Yunnan. Journal of Geophysical Research: Solid Earth, 127(1), e2021JB022710.

Steidl, J., Catchings, R., & Allam, A. (2019), RAMP deployment of 3C nodal for July Searles Valley 2019 Earthquake [Data set]. International Federation of Digital Seismograph Networks. https://doi.org/10.7914/SN/3J_2019

Thakur, P., Huang, Y., & Kaneko, Y. (2020), Effects of low-velocity fault damage zones on long-term earthquake behaviors on mature strike-slip faults. Journal of Geophysical Research: Solid Earth, 125(8), e2020JB019587.

Thakur, P., & Huang, Y. (2021), Influence of fault zone maturity on fully dynamic earthquake cycles. Geophysical Research Letters, 48(17), e2021GL094679.

Thompson, E. M. (2018), An Updated Vs30 Map for California with Geologic and Topographic Constraints (ver. 2.0, July 2022). U.S. Geological Survey data release. https://doi.org/10.5066/F7JQ108S.

Trugman, D. T. (2020), Stress-drop and source scaling of the 2019 Ridgecrest, California, earthquake sequence. Bulletin of the Seismological Society of America, 110(4), 1859-1871.

University of Nevada, Reno. (1971), *Nevada Seismic Network* [Data set]. International Federation of Digital Seismograph Networks. https://doi.org/10.7914/SN/NN.

Wang, Y., Allam, A., & Lin, F. C. (2019), Imaging the fault damage zone of the San Jacinto fault near Anza with ambient noise tomography using a dense nodal array. Geophysical Research Letters, 46(22), 12938-12948.

Weng, H., Yang, H., Zhang, Z., & Chen, X. (2016), Earthquake rupture extents and coseismic slips promoted by damaged fault zones. Journal of Geophysical Research: Solid Earth, 121(6), 4446-4457.

Yang, H., Duan, Y., Song, J., Jiang, X., Tian, X., Yang, W., ... & Yang, J. (2020). Fine structure of the Chenghai fault zone, Yunnan, China, constrained from teleseismic travel time and ambient noise tomography. Journal of Geophysical Research: Solid Earth, 125(7), e2020JB019565.

Yang, H. (2015), Recent advances in imaging crustal fault zones: A review. Earthquake Science, 28, 151-162.

Yang, W., Peng, Z., Wang, B., Li, Z., & Yuan, S. (2015), Velocity contrast along the rupture zone of the 2010 Mw6. 9 Yushu, China, earthquake from fault zone head waves. Earth and Planetary Science Letters, 416, 91-97.

Zhang, Y., Yang, H., Yang, W., Wang, W., & Ma, X. (2023). Along-Strike Variation in the Shallow Velocity Structure beneath the Chenghai Fault Zone, Yunnan, China, Constrained from Methane Sources and Dense Arrays. Seismological Research Letters, 94(5), 2273-2290.

Zhao, P., & Peng, Z. (2008), Velocity contrast along the Calaveras fault from analysis of fault zone head waves generated by repeating earthquakes. Geophysical Research Letters, 35(1).

Zheng, X., Zhao, C., Qiu, H., Niu, F., & Zhao, C. (2022), Velocity Contrast across the Zhaotong-Ludian Fault in Southwest China from the Analysis of Fault Zone Head Waves and Teleseismic P-Wave Arrivals. Seismological Society of America, 93(5), 2740-2752.

Zhou, Z., Bianco, M., Gerstoft, P., & Olsen, K. (2022), High-Resolution Imaging of Complex Shallow Fault Zones Along the July 2019 Ridgecrest Ruptures. Geophysical Research Letters, 49(1), e2021GL095024.